Plasma Phys. Control. Fusion **51** (2009) 014003 (10pp) doi:10.1088/0741-3335/51/1/014003

Study of direct-drive capsule implosions in inertial confinement fusion with proton radiography

C K Li[1], F H Séguin[1], J A Frenje[1], M Manuel[1], R D Petrasso[1], V A Smalyuk[2], R Betti[2,3], J Delettrez[2], J P Knauer[2], F Marshall[2], D D Meyerhofer[2,3], D Shvarts[2,4], C Stoeckl[2], W Theobald[2], J R Rygg[5], O L Landen[5], R P J Town[5], P A Amendt[5], C A Back[6] and J D Kilkenny[6]

[1] Plasma Science and Fusion Center, Massachusetts Institute of Technology, Cambridge, MA 02139, USA
[2] Laboratory for Laser Energetics, University of Rochester, Rochester, NY 14623, USA
[3] Department of Mechanical Engineering, Physics and Astronomy, University of Rochester, Rochester, NY 14623, USA
[4] NRCN, Negev and Ben Gurion University of the Negev, Beer-Sheva 84015, Israel
[5] Lawrence Livermore National Laboratory, Livermore, CA 94550, USA
[6] General Atomics, San Diego, CA 92186, USA

Received 26 June 2008, in final form 30 July 2008
Published 9 December 2008
Online at stacks.iop.org/PPCF/51/014003

Abstract

Implosions of spherical and cone-in-shell targets in direct-drive inertial confinement fusion (ICF) are studied with proton radiography. Time-gated, 15 MeV proton images provide a unique and comprehensive picture of ICF implosions that cover all the implosion phases from acceleration, through coasting, deceleration to stagnation. A self-generated internal radial electric field that reserves the direction during the course of implosions is observed. It is initially directed inward (at $\sim 10^9$ V m^{-1}), eventually reverses direction ($\sim 10^8$ V m^{-1}) and is probably the consequence of the electron pressure gradient. Monte Carlo simulations quantitatively confirm the observations of the electric field and its evolution. The observations are compared with self-emitted x-rays and hydrodynamic simulations.

(Some figures in this article are in colour only in the electronic version)

1. Introduction

Achieving ignition and high gain is the ultimate goal of inertial confinement fusion (ICF) research [1–4]. This requires that a cryogenic deuterium–tritium (DT) filled spherical capsule be symmetrically imploded to reach sufficiently high temperature and density. In the direct-drive approach to ICF this occurs in response to a large number of high-power, individual laser beams illuminating the surface of a capsule [1–4]. There are currently two major schemes for target ignition which are being studied: the first, the conventional 'hot spot' ignition scheme

for which the formation of two different regions occurs as a consequence of capsule implosion: a small mass of low density, hot fuel at the center surrounded by a larger mass of high density, low temperature fuel. Shock coalescence 'ignites' the hot spot, and a self-sustaining burn wave propagates into the main fuel region. The second approach to target ignition [5], the 'fast ignition' scheme, involves a pre-compressed target being ignited by an external 'spark'. Since fast ignition separates capsule compression from hot spot formation, this method may relax the conditions on target compression and reduce the total energy requirements for ICF ignition, leading to higher target gain [5].

Successful ICF implosion requires the understanding and controlling of implosion dynamics, which have been studied experimentally with a number of diagnostics. Conventional x-ray diagnostics (the measurements of x-rays from either self-emission or backlighting [6, 7]) are very valuable, but do not directly provide information about mass assembly (areal density (ρR)) or self-generated electric (E) and magnetic (B) fields. Measurements of self-emitted fusion products, such as neutrons and charged particles, provide information about conditions at nuclear bang time but are not very useful for studying dynamics earlier or later [8–13].

In this paper we present unique nuclear observations of capsule implosions of direct-drive spherical and cone-in-shell targets on the OMEGA laser facility [14], using a novel method of monoenergetic proton radiography [15–20]. This technique allows the distributions of self-generated $E + B$ fields, the ρR by measuring the energy loss of backlighting protons, for all phases of the implosion to be obtained. The radiographic data are contrasted with the x-ray images and hydrodynamic simulations. An earlier work by Mackinnon *et al* [21] successfully demonstrated the feasibility of imaging implosions with protons (produced by laser–plasma interactions), backlighting plastic (CH) capsules that were imploded by six 1 μm wavelength laser beams. They reported no fields inside and surrounding the capsule, in contrast to the observations shown here, and this is not presently understood.

This paper is structured as follows: section 2 describes the experiments and section 3 presents the experimental data. The results are discussed in section 4 and summarized in section 5.

2. Experiments

The experiment is illustrated schematically in figure 1. A subject spherical CH capsule or a cone-in-shell target is driven directly with 36–40 beams of frequency-tripled (0.35 μm) UV light. The targets are ~860 μm in diameter, 20–24 μm thick shells and are all filled with 15 atm H_2 gas. The laser pulse is square, with a duration of 1 ns and a total energy of ~14–16 kJ. The individual laser beams are smoothed using a single-color cycle, 1 THz two-dimensional (2D) smoothing by dispersion (SSD) plus polarization smoothing (PS) [22, 23].

Implosions are backlit with monoenergetic protons (fusion products from nuclear reaction $D + {}^3He \rightarrow \alpha + p$ (14.7 MeV)), generated from D^3He-filled, exploding-pusher implosions, which are driven by 16–20 Ω laser beams [15, 19, 20]. The duration of the backlighter is ~130 ps, and the timing of the implosion laser is adjustable relative to the times that the backlighting protons arrive at the implosions. The implosions are imaged with self-emitted x-rays from the directions nearly perpendicular to the backlighting protons by framing cameras.

Each image contains both spatial and energy information, because the CR-39 detectors record the position and energy of every individual proton. The images can be displayed to show either proton fluence versus position or proton mean energy versus position, providing important information about field distributions and capsule compression. Several sources of image broadening can compromise the fidelity of the radiography images. There are broadening radii R_p, R_{sc} and R_d due to finite backlighter size (r_s), scattering at the subject

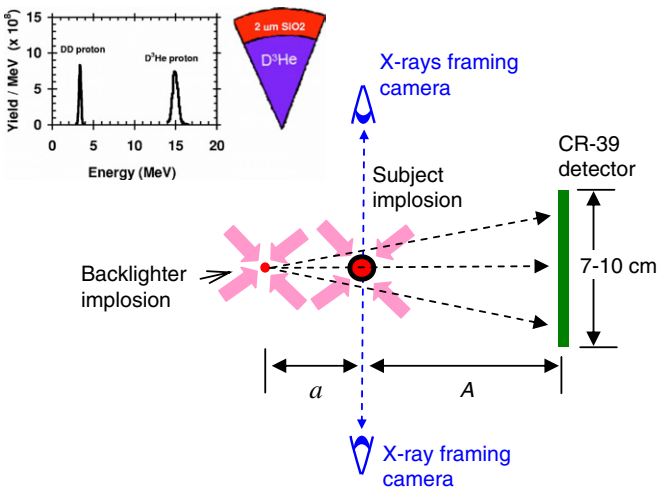

Figure 1. Experimental setup. Shown are proton backlighter, subject implosion (either a spherical or a cone-in-shell target), imaging detectors and x-ray framing cameras. Typical yields are $\sim 2 \times 10^8$ for D^3He protons. A typical proton spectrum measured with a charged-particle spectrometer indicates that both nuclear lines are upshifted slightly from their birth energies because of capsule charging.

(θ_{sc}) [25] and broadening in the detector (r_d), respectively [15]. The net effect of these processes is the convolution of the image structure by the Gaussian $\exp(-r^2/R_{tot}^2)$, where $R_{tot} = \sqrt{R_p^2 + R_d^2 + R_{sc}^2}$ and the characteristic image broadening radii $R_p = A(a + A)^{-1} r_s$, $R_{sc} = aA(a + A)^{-1}\theta_{sc}$ and $R_d = a(a + A)^{-1} r_d$. A and a are shown in figure 1. The effective FWHM of the backlighter is $\approx 40\,\mu$m [15–20], the primary limit on the intrinsic spatial resolution of the imaging system. In images of imploded capsules, the spatial resolution is degraded somewhat by scattering of the imaging protons as they pass through the capsules.

3. Data

Figure 2 shows radiographic images of two snap shots made perpendicular to the Au cone axis with 15 MeV D^3He protons for cone-in-shell targets before and during implosion, proton fluence in figure 2(a) and energy in figure 2(b), respectively. Several important features are apparent in these images. First, the character of the isotropic and monoenergetic proton source is reflected in the uniform background; second, a complex filamentary structure is seen in the fluence image of $t = 1.58$ ns (this paper focuses on the region inside a target while the area outside this region is the subject of another study of external fields [24]). Third, substantial plasma blowoff from the cone casts a much wider shadow as the capsule is imploded. Fourth, a substantial enhancement of the proton fluence at the center of the imploded target suggests the presence of a radially directed, focusing E field. And finally, radial compression of the capsule by a factor of 2 is seen in figure 2(b). As a comparison, a time-integrated soft x-ray image taken using a pinhole camera is shown in figure 2(c).

Figure 3 shows proton radiographs of spherical implosions at different times with proton fluence (figure 3(a)) and energy (figure 3(b)). In the uncompressed case ($t = 0.0$ ns) the protons that passed through the shell limb lost the most energy, resulting in the dark ring of (b), and were scattered the most, resulting in the light ring of (a). The soft x-ray images

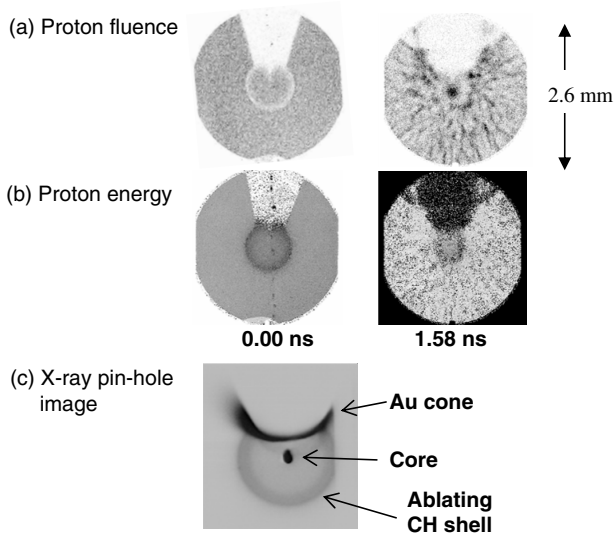

Figure 2. Images of proton fluence (*a*) and energy (*b*) of a spherical CH capsule with attached gold cone (at $t = 0.0$ and ~1.6 ns, where $t = 0.0$ ns means the target is not driven). In (*a*), darker means higher fluence, while in (*b*) darker means lower proton energy (more matter traversed). The gray-scale mapping is different for each image, to account for different backlighter yields and make the most important structure clearly visible. Figure 2(*c*) shows a time-integrated x-ray pinhole image.

with ~60 ps step exposures taken using framing cameras are shown in figure 3(*c*) and indicate the temporal evolution of the size and shape of the capsule outer boundary. A striking feature in figure 3(*a*) is that a strong central peak appears in the image during the early stage of implosion ($t \sim 0.6$ ns) while a central dip appears at a later time ($t \sim 1.6$ ns). As shown in figure 4 from [20], the lineouts of the two typical images (indicating the radial profiles of proton fluence) provide the compelling evidence of such a fluence peak at an earlier time ($t = 0.8$ ns) and fluence dip at a later time ($t = 1.9$ ns). To clearly demonstrate that these proton fluence peaks and dips do not depend on where the detector was placed (i.e. at some special distances from the backlighter in the context of our experiment configuration), Monte Carlo calculations are performed. The results shown in figure 5 indicate that for a given amount of deflection, the focus or defocus of the image is relatively insensitive to the specific distance of the detector position.

4. Results and discussions

Two types of information of the implosion are inferred from the previous images: first, quantitative information about the implosion-associated fields through the spatial distribution of proton fluence (fluence peak or dip due to deflections of proton trajectories) and, second, quantitative information about capsule sizes (R) and areal densities (ρR), as illustrated in figure 6. The details are discussed below.

4.1. A self-generated radial electric field

The striking features of the proton fluence peak and dip demonstrated quantitatively in figure 4, as discussed below, cannot be accounted by proton scattering. These features result from the deflection of proton trajectories by radial electric fields. At earlier times the field must have

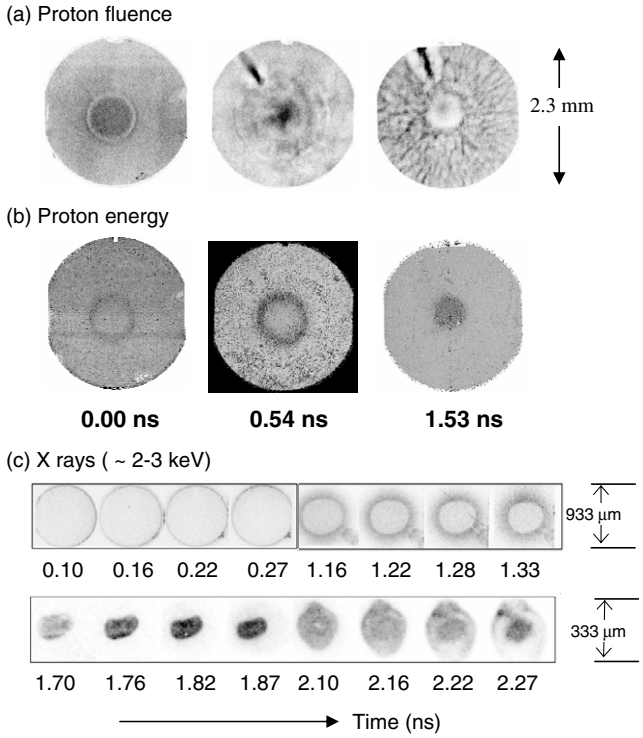

Figure 3. Proton radiographs of spherical implosions, (*a*) and (*b*), at different times, illustrating the time evolution of mass distribution and radial E field (*a*). The capsule-mounting stalk appears in the upper left corner of each fluence image. (*c*) The soft x-ray images with a ∼60 ps step exposure show the temporal evolution of the size and shape of the capsule outer boundary.

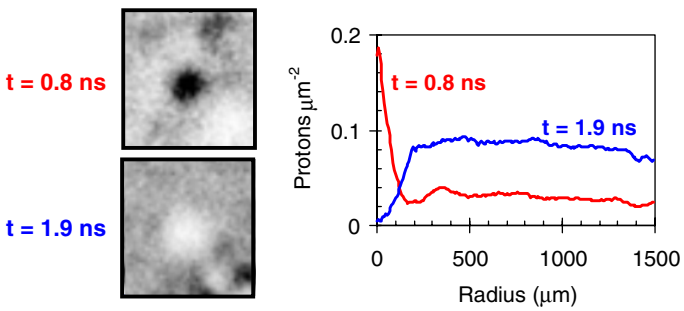

Figure 4. Radial profiles of the proton fluence images at $t = 0.8$ ns and 1.9 ns. A fluence peak occurs in the image centers during the early stages of a spherical implosion, indicating a 'focusing' of imaging protons there; in contrast, the fluence is extremely low, or defocused, at the image centers at later times. Note that the different levels ($\times \sim 2$) of the proton fluence outside the capsules ($r > \sim 200\,\mu$m) are due to the variations from the backlighter proton yields.

been centrally directed in order to focus the protons passing through the capsule shell toward the center of the imaging detector. To account for the rapid change from a central fluence peak to a central fluence dip at ∼1.5 ns, the radial field must have either reversed direction or suddenly become at least three times larger at that time (as shown by Monte Carlo simulations [20]), in which case protons would have struck the detector outside the shadow of the capsule.

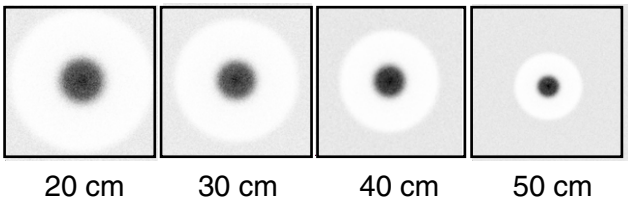

Figure 5. Monte Carlo simulation of the proton fluence images at the detector plane at different distances. This shows that, for a spherical implosion, the observed effect of proton fluence peaked at the target center region is relatively insensitive to the specific distance of the detector position.

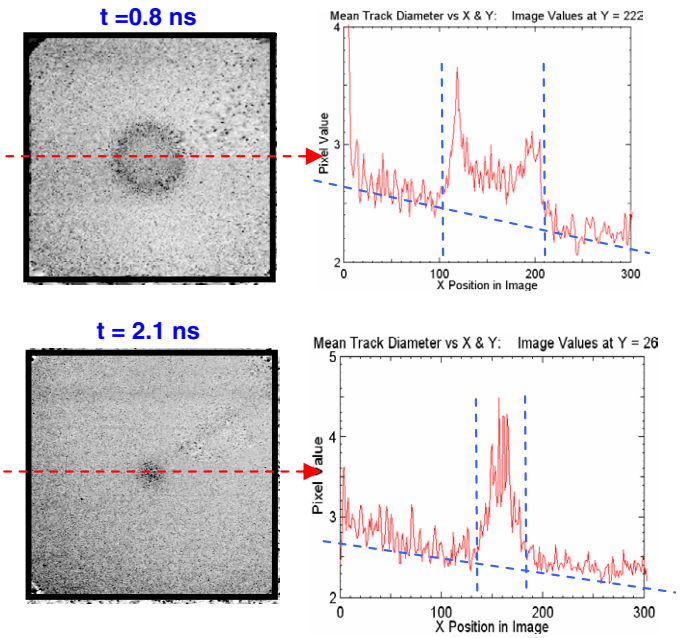

Figure 6. Illustration of lineouts through the centers of each of the individual proton energy images of a spherical implosion; the mean width provides the averaged capsule size ($\approx 2R$), while the mean height indicates the total ρL ($\approx 2 \times \rho R$).

To demonstrate that radial fields are necessary to explain the central peaks and dips in image fluence, Monte Carlo simulations of image formation were conducted for the imaging geometry and backlighter yields, etc, using the density distributions predicted by hydrodynamic simulations. Images simulated with the assumption that there were no radial E fields, and that proton trajectories were deflected by scattering occurring in the capsule shell limbs, are shown in figure 7. Although scattering affects these images, it does not lead to peaks and dips of the sizes observed in the data. Images simulated with the assumption that there is a radial E field pointing to the center at $t = 0.8$ ns, but pointing away from the center at $t = 1.9$ ns, are shown in figure 8. At $t = 0.8$ ns there is a fluence peak in the center, while at $t = 1.9$ ns there is fluence dip in the center. Both features mimic the above experimental results with approximately equal amplitudes (figure 4) and provide compelling evidence that there is a radial E field and its direction reverse. These comparisons are qualitative and/or semi-quantitative because simulations are static while the measurements were dynamic within a period of time of the backlighter nuclear burn.

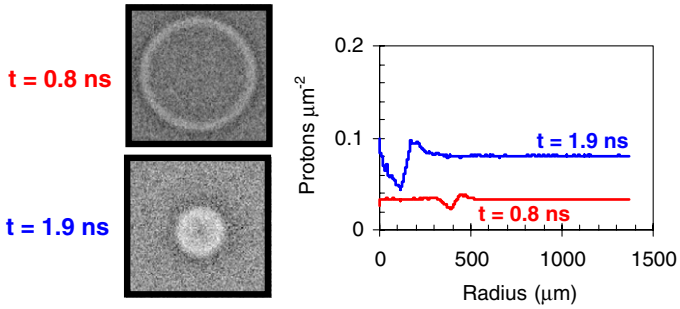

Figure 7. Monte Carlo simulations proton fluence distribution of a spherical implosion caused by scattering only. It is shown that there is neither fluence peak at 0.8 ns nor fluence dip at 1.9 ns.

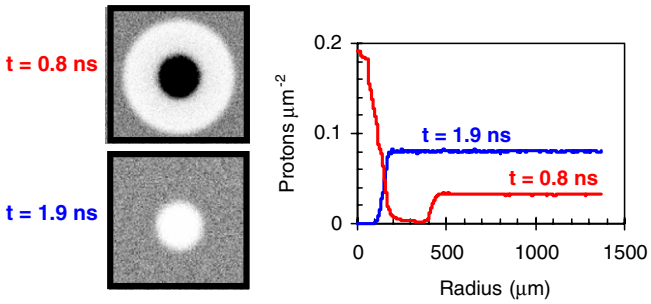

Figure 8. Monte Carlo simulations (with scattering + radial E field; field direction reversed for $t = 1.9$ ns). A fluence peak occurs in the image centers during the early stages of a spherical implosion, indicating a 'focusing' of imaging protons there; in contrast, the fluence is extremely low, or defocused, at the image centers at later times. Note that the different levels ($\times \sim 2$) of the proton fluence outside the capsules ($r > \sim 200\,\mu$m) are due to the variations from the backlighter proton yields.

The E-field source that is consistent with the data is the gradient of plasma electron pressure ($E \approx -\nabla p_e/en_e$) [26] (other possible sources do not fit as naturally with the data [20]). The pressure gradient has the correct sign at earlier times and reverses direction at approximately the correct time. This is illustrated by the electron pressure and density profiles from 0.8 to 2.1 ns, calculated using the LILAC hydrodynamic simulation code [27] and are shown in figure 9. Using calculated ∇p_e and n_e at different times, the resultant strength of E is estimated as being in the range $\sim -10^9$ to $\sim 10^8$ V m^{-1}. The strength of E field can be approximately estimated from the measured proton trajectory distortion [20]. The predictions match the data in three crucial ways: the field strength and sign before the reversal ($\sim -10^9$ V m^{-1}, directed inward), the time of the field reversal ($\sim$1.5 ns) and the field strength after the reversal ($\sim 10^8$ V m^{-1} directed outward). The detailed structures of the fluence images are modified in ways that do not affect our conclusions, by the in-flight movement of the shell ($V_{imp} \sim -2.5 \times 10^7$ cm s^{-1}), which is $\sim 30\,\mu$m during the backlighter nuclear burn time ($\sim$130 ps.)

4.2. Areal density of implosion dynamics

Figure 3(*b*) shows the diameter-averaged D^{3}He proton images at different implosion times. The dark area represents the regions with larger proton diameters (and therefore lower energies), resulting from the energy loss of protons passing through the different parts

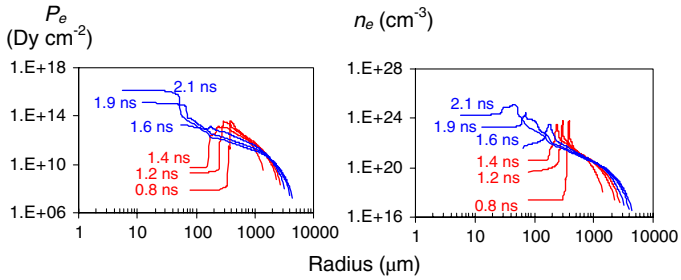

Figure 9. The profiles of the electron pressure of a spherical implosion at different times. It is shown that the gradients of the radial pressures are positive ($\nabla p_e > 0$) for early stages of implosions ($t = 0.8$, 1.2 and 1.4 ns), but are negative ($\nabla p_e < 0$) for later stages of implosions ($t = 1.6$, 1.9 and 2.1 ns).

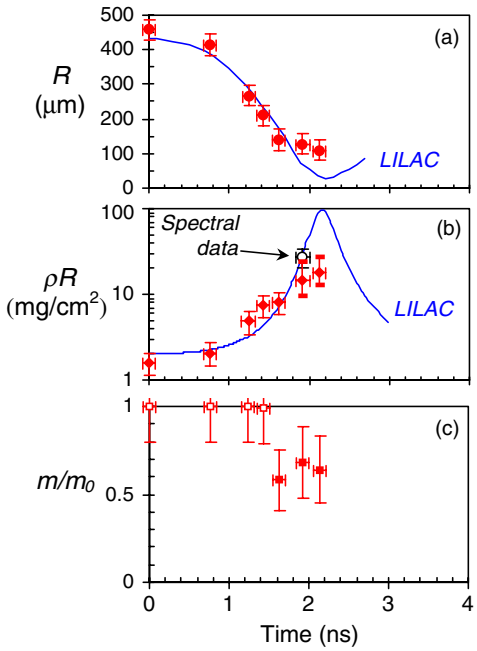

Figure 10. Measured capsule radius (solid cycles, (*a*)) and ρR (solid diamonds (*b*)) compared with LILAC 1D simulations (solid lines) for spherical implosions. The uncertainties in the x axis represent the nuclear burn time. ρRs at 1.9 and 2.1 ns in (*b*) are actually the lower limits, with large error bars resulting from the uncertainties of mean track diameters and the conversions to proton energy loss. Scattering plays an important role leading to such uncertainties. In contrast, the error bars at other times represent typical ρR asymmetries ($\sim \pm 20\%$). A data point (open diamond in (*b*)) represents the mean $\rho R \approx 25\,\mathrm{mg\,cm^{-2}}$ ($\sim$90% of 1D calculation) at bang time, as measured by several proton spectrometers in different directions. (*c*) Measured time-dependent mass ablations. The large error bars at the later times (solid squares) reflect the uncertainty of the above R and ρR measurements.

of an imploded capsule, leading to the determination of the target ρR ($\approx 0.5\rho L$, where $\rho L = \int_{E_0}^{E} \rho(\mathrm{d}E/\mathrm{d}x)^{-1}\,\mathrm{d}E$ [28, 29] and L is the proton path length). As indicated in figure 6 quantitative information about the sizes and ρRs at different times can be extracted from the lineout through the centers of individual images. The measurements are contrasted with LILAC simulations in figure 10 [20]. The simulations come reasonably close to matching

the observed evolution of capsule convergence and ρR during the acceleration and coasting phases (∼0–1.6 ns), but predict somewhat smaller values of radius, and larger values of ρR, than those measured at the times of nuclear burn (∼1.9 ns) and peak compression (∼2.1 ns). This indicates that the implosions had approximately 1D performance, with little impact from hydrodynamic instabilities, before deceleration. It has been suggested that the performance approaches 1D because of full single-beam smoothing, which significantly improves the shell integrity during the acceleration phase, and due to thickening of the shell during subsequent coasting which further enhances shell integrity [23]. The apparent degradation of capsule performance at later times relative to the 1D simulation may be largely a consequence of fuel-shell mixing and implosion asymmetry [11, 12].

Proton data are qualitatively verified by x-ray images of self-thermal emissions (∼2–3 keV that allows a full survey of target compression and rebound, see figure 3(*c*)). X-ray images show that the shape of the outer boundary of a capsule evolves asymmetrically to form elongated images before the peak compression (∼2.1 ns), then rebounds along the perpendicular direction. Since x-ray images are taken from the direction images nearly perpendicular to the backlighting protons (the proton images all had a round shape), such an elongation suggests that the implosions were asymmetric as a result of more laser irradiation coming from poles than that from the equator. The sizes of x-ray images are slightly smaller than the sizes of proton images which may indicate the effects of proton scattering.

The residual mass during the implosion process can be estimated in terms of the measured R and measured ρR: $m/m_0 \approx C_r^{-2}\rho R(t)/\rho R(0)$, where $C_r \equiv R(0)/R(t)$ is the target convergence ratio. Figure 10(*c*) indicates that ∼30–40% of the shell has been ablated by bang time. Although the mass estimates have large uncertainties due to their association with both R and ρR measurements, they are helpful for illustrating the dynamics of mass ablation during implosions.

5. Summary

In summary, we have conducted the first measurements of ICF implosion dynamics of spherical and cone-in-shell targets using time-gated, monoenergetic proton radiography. Critical information inferred directly from proton images uniquely characterizes the spatial structure and temporal evolution of imploded capsules that was hitherto unavailable using conventional measurements. To quantitatively delineate these measurements, data are contrasted with both self-emitted x-rays and hydrodynamic simulations. Variation of proton fluence inside the imploded targets during implosions unambiguously reveals the direction reversal of a self-generated radial electric field; this new observation is demonstrated to be a probable consequence of the reversal of the electron pressure gradient.

Acknowledgments

The work described here was performed at the LLE National Laser User's Facility (NLUF) and was supported in part by US DOE (Grant No DE-FG03-03SF22691), LLE (subcontract Grant No 412160-001G), LLNL (subcontract Grant No B504974), the Fusion Science Center at University of Rochester and GA under DOE (DE-AC52-06NA27279).

References

[1] Nuckolls J *et al* 1972 *Nature* **239** 139
[2] Lindl J D 1999 *Inertial Confinement Fusion* (New York: Springer)

[3] Atzeni A and Meyer-Ter-Vehn J 2004 *The Physics of Inertial Fusion* (Oxford: Clarendon)
[4] McCrory R *et al* 2008 *Phys. Plasmas* **15** 055503
[5] Tabak M *et al* 1994 *Phys. Plasmas* **1** 1626
[6] Marshall F J *et al* 2004 *Phys. Plasmas* **11** 251
[7] Craxton R S *et al* 2005 *Phys. Plasmas* **12** 056304
[8] Shiraga H *et al* 1980 *Appl. Phys. Lett.* **37** 602
[9] Séguin F H *et al* 2003 *Rev. Sci. Instrum.* **74** 975
[10] Disdier L *et al* 2006 *Phys. Plasmas* **13** 056317
[11] Li C K *et al* 2002 *Phys. Rev. Lett.* **89** 165002
[12] Li C K *et al* 2004 *Phys. Rev. Lett.* **92** 205001
[13] Frenje J A *et al* 2004 *Phys. Plasmas* **11** 2798
[14] Soures J M *et al* 1996 *Phys. Plasmas* **3** 2108
[15] Li C K *et al Rev. Sci. Instrum.* **77** 10E725
[16] Li C K *et al* 2006 *Phys. Rev. Lett.* **97** 135003
[17] Li C K *et al* 2007 *Phys. Rev. Lett.* **99** 015001
[18] Li C K *et al* 2007 *Phys. Rev. Lett.* **99** 055001
[19] Rygg J R *et al* 2008 *Science* **319** 1223
[20] Li C K *et al* 2008 *Phys. Rev. Lett.* **100** 225001
[21] Mackinnon A *et al* 2006 *Phys. Rev. Lett.* **97** 045001
[22] Skupsky S *et al* 1999 *Phys. Plasmas* **6** 2157
[23] Meyerhofer D D *et al* 2001 *Phys. Plasmas* **8** 2251
[24] Séguin F H *et al* in preparation
[25] Highland V L 1975 *Nucl. Instrum. Methods* **129** 497
[26] Braginskii S I 1965 *Review of Plasma Physics* (New York: Consultant Bureau)
[27] Deletrezz J *et al* 1987 *Phys. Rev.* A **36** 3926
[28] Li C K and Petrasso R D 1993 *Phys. Rev. Lett.* **70** 3059
[29] Li C K *et al* 2000 *Phys. Plasmas* **7** 2578